Electronic and Spin-State Effects on Dinitrogen Splitting to Nitrides in a Rhenium Pincer System

Jeremy E. Weber,[a] Faraj Hasanayn,[b] Majed Fataftah,[a] Brandon Q. Mercado,[a] Robert H. Crabtree,[a] and Patrick L. Holland[,a]*

[a] Department of Chemistry, Yale University, 225 Prospect Street, New Haven, Connecticut 06511.

[b] Department of Chemistry, American University of Beirut, Beirut 1107 2020, Lebanon.

Abstract: Bimetallic nitrogen (N_2) splitting to form metal nitrides is an attractive method for N_2 fixation. Though a growing number of pincer-supported systems can bind and split N_2, the precise relationship between ligand properties and N_2 binding/splitting remains elusive. Here we report the first example of an N_2-bridged Re^{3+} complex, $[(trans\text{-}P_2{}^{tBu}Pyrr)ReCl_2]_2(\mu\text{-}\eta^1\text{:}\eta^1\text{-}N_2)$ ($P_2{}^{tBu}Pyrr$ = $[2,5\text{-}(CH_2P{}^tBu_2)_2C_4H_2N]^-$). In this case, N_2 binding occurs at a higher oxidation level than in other reported pincer analogues. Analysis of the electronic structure through computational studies shows that the weakly π-donor pincer ligand stabilizes an open shell electronic configuration that leads to enhanced binding of N_2 in the bridged complex. Utilizing SQUID magnetometry, we demonstrate a singlet ground state for this Re–N–N–Re complex, and we offer tentative explanations for the antiferromagnetic coupling of the two local S = 1 sites. Reduction and subsequent heating of the rhenium(III)–N_2 complex leads to chloride loss and cleavage of the N–N bond with isolation of the terminal rhenium(V) nitride complex, $(P_2{}^{tBu}Pyrr)ReNCl$.

INTRODUCTION

Transition metal N_2 complexes have been crucial in elucidating the various elementary steps involved in N_2 functionalization.[1] N_2 can bind to one or more metals, with the linear bimetallic (μ–η^1:η^1) binding mode being particularly common for metals in groups 5–8 of the transition series.[2] In some cases, this binding is followed by N_2 splitting through homolytic cleavage of the N–N triple bond to form two nitride complexes (Figure 1).[3] This six-electron reduction requires a pair of transition metals that are each capable of the required three-electron change of oxidation state. In 1995, the Cummins group demonstrated that N_2 splitting was possible by reducing N_2 cooperatively with two Mo^{3+} complexes to give two equivalents of a terminal Mo^{6+} nitrido complex.[4] Later thermochemical studies demonstrated that, in this system, splitting the triple bond of N_2 (226 kcal/mol) is counterbalanced by the formation of two strong Mo–N triple bonds (155 kcal/mol each).[5-6] Computational studies indicated that cleavage proceeds through a zigzag M–N–N–M transition state (TS), and molecular orbital (MO) correlation diagrams revealed that this kinetically facile reaction requires a specific electronic configuration with ten electrons in the M–N–N–M π orbital manifold.[7-8] While the Cummins system can cleave N_2 in the absence of any exogenous reagents, other N_2-bridged molybdenum complexes either do not cleave N_2[9-10] or require some trigger such as reduction,[11-13] oxidation,[14] protonation,[15] or irradiation.[16] These reports span vastly different ligand environments, and the general principles governing the N_2 splitting reaction are not yet clear.

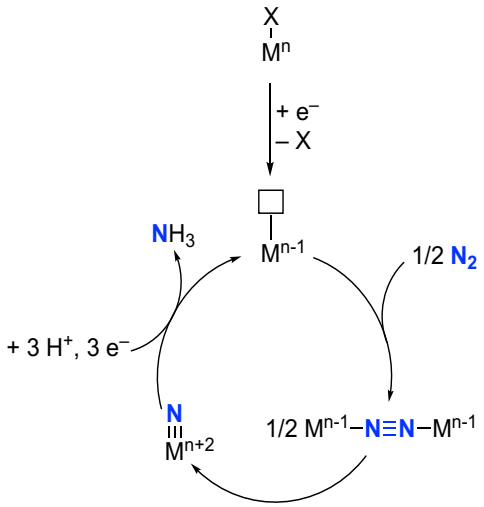

Figure 1. N_2 activation through an N_2 splitting mechanism

Molybdenum complexes have been the most extensively studied for N_2 splitting, but interest has increasingly moved to rhenium complexes. Although rhenium-N_2 complexes have been known since the late 1960s, N_2 splitting by rhenium complexes has been reported only recently.[17] In their seminal work, Schneider and coworkers reported that when the Re^{3+} complex $(PNP^{tBu})ReCl_2$ (PNP^{tBu} = $N(CH_2CH_2P(^tBu)_2)_2^-$) is reduced to the Re^{2+} oxidation state, it can bind and split N_2 to form the terminal Re^{5+} nitrido complex, $(PNP^{tBu})ReNCl$.[18] In a related study, $(HPNP^{iPr})ReCl_3$ ($HPNP^{iPr}$ = $HN(CH_2CH_2P(^iPr)_2)_2$) proved capable of generating N_2-derived organic products by combining electrochemical and photochemical steps.[19] More recently, Bruch *et al.* demonstrated distinctly different Re–N_2 chemistry with PONOP (PONOP = 2,6-bis-(diisopropylphosphinito)pyridine) pincer complexes.[20] When reduced to the Re^{2+} oxidation state, this system binds N_2, but subsequent N_2 splitting required photolysis. When the resulting nitrido complex, *cis*-$(PONOP)ReNCl_2$, was treated with SmI_2 and water, stoichiometric quantities of NH_3 were formed. Although these reports highlight a new class of reactivity for rhenium complexes, the difference in behavior of apparently similar pincer ligand environments warrants further

investigation. Specifically, the relationship between electronic structure of the ligand environment and N_2 splitting remains to be understood.

Here, we report the synthesis and reactivity of a series of rhenium complexes bearing the $P_2^{tBu}Pyrr$ pincer ligand ($P_2^{tBu}Pyrr$ = (2,5-{$^tBu_2PCH_2$}$_2C_4H_2N$)$^-$).[21] Complexes bearing $P_2^{tBu}Pyrr$ have been studied for a variety of reactions, including N_2 reduction.[22-28] Insights from magnetic and computational studies reported herein indicate that the N_2 reactivity of rhenium complexes bearing $P_2^{tBu}Pyrr$ is influenced by the weaker π-donor ligand environment and differs from the previously studied PNP^{tBu} pincers that have a dialkylamido π-donor. When the $P_2^{tBu}Pyrr$-supported rhenium-dinitrogen complexes are reduced to Re^{2+}, we show that the N_2 ligand cleaves to form a pair of terminal Re^{5+} nitride complexes. These complexes provide new insights into the correlations between the ligand identity, the electronic structure at rhenium, and the reactivity of bound N_2.

RESULTS

Synthesis and Characterization of Re^{3+} Complexes. Heating a 1:1 mixture of $ReCl_3(py)_2PPh_3$ and $Li(P_2^{tBu}Pyrr)$ in tetrahydrofuran (THF) at 80 °C for 8 h resulted in the formation of a new species as the major product, as assessed by ^1H and ^{31}P NMR spectroscopy. This product features six ^1H resonances and one ^{31}P resonance. The ^1H NMR spectrum spans ~25 ppm, and the signal in the $^{31}P\{^1H\}$ NMR spectrum lies at –1620 ppm, which is characteristic of temperature independent paramagnetism (TIP) in d^4 octahedral Re^{3+} complexes (Figures S1–S2).[29-30] Single-crystal X-ray diffraction (XRD) identified the product as the six-coordinate complex *trans*-($P_2^{tBu}Pyrr$)$ReCl_2$(py) (**1a–py**), which was isolated in 61% yield (Chart 1). Asymmetric puckering of the methylene linkers in the ligand backbone results in the loss of a

mirror plane, forming two C_2-symmetric conformers that interconvert rapidly on the NMR timescale.

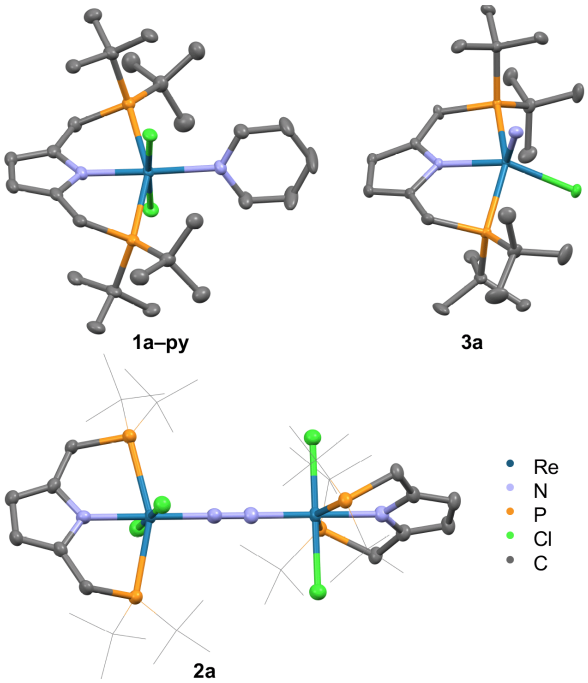

Chart 1. Solid-state structures of complexes **1a–py**, **2a**, and **3a** with thermal ellipsoids at 50% probability. Hydrogen atoms are omitted for clarity. The ^{t}Bu groups of complex **2a** are displayed as wireframes for clarity.

Scheme 1. Abstraction of Pyridine From a Rhenium(III) Precursor

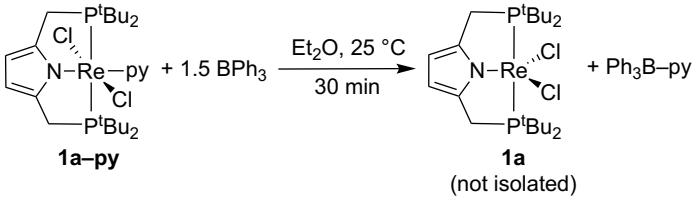

The Re center in **1a–py** is coordinatively saturated and does not react with N_2. To facilitate N_2 binding, **1a–py** was added to a solution of excess BPh_3 in diethyl ether (Et_2O) or benzene, which led to a color change from yellow to green, and precipitation of Ph_3B–py (Scheme 1). Monitoring the reaction mixture by ^{1}H NMR spectroscopy in benzene-d_6 indicated the disappearance of **1a–**

py and the formation of a new, C_{2v}-symmetric species in 87% spectroscopic yield (Figure S5). The ^{1}H and $^{31}P\{^{1}H\}$ NMR spectra are consistent with the formation of (P_2^{tBu}Pyrr)$ReCl_2$ (**1a**) because the spectra resemble those of other diamagnetic five-coordinate rhenium(III) compounds (Figures S3–S4).[18] Attempts to isolate **1a** as a crystalline solid under Ar were unsuccessful, but brown crystals suitable for single crystal XRD grew from a solution of **1a** under N_2 at –40 °C. The XRD data indicate that the isolated material is [*trans*-(P_2^{tBu}Pyrr)$ReCl_2$]$_2$(μ-η^1:η^1-N_2) (**2a**; Chart 1), an S_4-symmetric complex with a Re–N–N–Re bridge. The N–N bond distance (1.115(7) Å) indicates that the bridging N_2 ligand of **2a** is only slightly activated.[31] A resonance Raman spectrum of solid **2a** using λ_{ex} = 532 nm shows bands at 1862, 1819, and 1719 cm^{-1} that are absent in a sample crystallized under $^{15}N_2$, which instead exhibits new Raman signals at 1830, 1758, and 1695 cm^{-1} (Figure S27). The presence of multiple isotope-sensitive bands, and the small isotope shift, suggest that the observed signal is not an isolated diatomic N–N stretching mode, and that the normal mode has contributions from ligand motion. The coupling between N_2 and other motions prevents us from using the vibrational frequency as a gauge of N–N bond weakening. In contrast, an overlay of the IR spectra of **2a** and **2a–$^{15}N_2$** (Figure S23) highlights that all resonances are within 2 cm^{-1} of one another except for a signal at 536 cm^{-1} in **2a** that shifts to 519 cm^{-1} in **2a–$^{15}N_2$**. The observed 17 cm^{-1} bathochromic shift is in agreement with the harmonic oscillator approximation for a Re–N stretching mode. Therefore, this mode is assigned as the antisymmetric combination of the Re–N(N_2) stretches, which is IR active.

Scheme 2. Reversible N_2 Binding by **1a** Gives Bridging **2a**

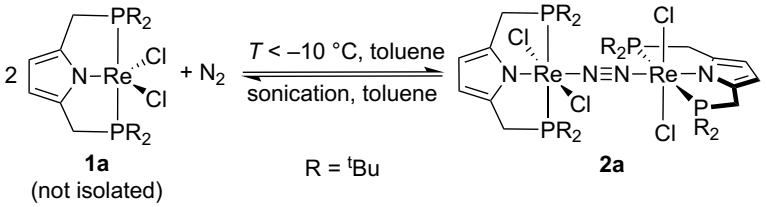

1a
(not isolated)

2a

Complex **2a** is insoluble in organic solvents, which limited spectroscopic characterization. Sonicating crystalline **2a** in organic solvents (THF, Et_2O, benzene and toluene) led to green solutions. When **2a** was sonicated in C_6D_6, the ^1H and $^{31}P\{^1H\}$ NMR spectra of the resulting solution indicated the formation of a single species with resonances that match **1a** discussed above. Thus, we concluded that N_2 dissociates from **2a** readily upon sonication in solution (Scheme 2). To investigate the reversibility of N_2 binding to **1a** at low temperatures, we collected electronic absorption spectra of **1a** in toluene under 1 atm of N_2 at various temperatures. At room temperature, the absorption spectrum exhibits maxima at 309, 699, and 778 nm (Figures S16–S17). Cooling this solution to –78 °C led to the growth of new absorptions with maxima at 507 and 593 nm, which do not appear when the procedure is repeated under an atmosphere of Ar (Figure S18–19). Furthermore, when the solution is warmed to room temperature the absorbances at 507 and 593 nm disappear. These data are consistent with reversible N_2 binding to **1a**. Thermodynamic parameters were not determined owing to the partial precipitation of **2a** at lower temperatures.

Magnetism of Re^{3+} Complexes. To gain deeper insight into the electronic structure of the new complexes, we measured the temperature dependence of their magnetic susceptibilities. The temperature-dependent DC magnetic susceptibility (χ_M) for **1a–py** was collected from 2–200 K under an applied magnetic field of 1000 Oe. The value of χ_M for **1a–py** at 200 K is 3.5×10^{-4} cm^3/mol, and is temperature independent in the temperature range of 25–200 K (Figure S28). This behavior deviates from the Curie law, and the corresponding $\chi_M T$ values (for example, $\chi_M T = 0.07$ cm^3K/mol at 200 K) are significantly smaller than expected for $S > 0$ ground states (Figure S29). We propose that **1a–py** has a thermally isolated $S = 0$ ground state with TIP (as suggested by the NMR spectra described above), as well as a small paramagnetic impurity that explains the upward trajectory of χ_M below 25 K.

In contrast to **1a–py**, the magnetic susceptibility of **2a** displays a strong temperature dependence. Plotting $\chi_M T$ versus temperature results in a positive slope (Figure 2). At 300 K, **2a** has a $\chi_M T$ value of 1.25 cm^3K/mol, and this drops with decreasing temperature, approaching zero at 2 K. These data fit well to a model with two intermediate-spin Re^{3+} ($S_{Re} = 1$) centers that are antiferromagnetically coupled, which predicts $\chi_M T = 2$ cm^3K/mol in the high-temperature limit (which is not experimentally accessible). To quantify the magnitude of the antiferromagnetic exchange interaction, the $\chi_M T$ data were modelled using the spin Hamiltonian $\hat{H} = D(\hat{S}_{1z}^2 + \hat{S}_{2z}^2) + (g_1 + g_2)\mu_B \boldsymbol{SH} - 2J(\hat{S}_1 \cdot \hat{S}_2)$. In this Hamiltonian, D is the axial zero-field splitting parameter, g_1 and g_2 are the isotropic electron g-value, $\hat{S}_1$ and $\hat{S}_2$ are the spin operators, and J is the exchange interaction. The best fit to the $\chi_M T$ data was achieved with $J = -22(2)$ cm^{-1} (see SI for details and alternative simulations).

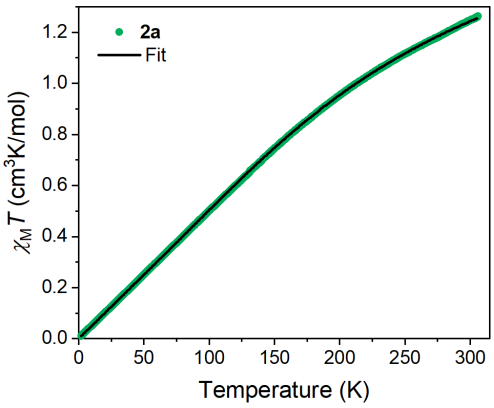

Figure 2. $\chi_M T$ data for **2a** (green) collected from 2–300 K under an applied magnetic field of 500 Oe. The data were simulated (black line) as two $S = 1$ subsites with $D = 350(20)$ cm^{-1} and $g_1 = g_2 = 1.72(12)$, with antiferromagnetic coupling of $J = -22(2)$ cm^{-1}. The fit includes an $S = {}^1/_2$ paramagnetic impurity (0.035%) and a TIP contribution of 5.6×10^{-4} cm^3/mol.

Influence of Supporting Ligand on Electronic Structure and Reactivity of Re^{3+} Complexes. To our knowledge, compound **2a** is the first isolable Re^{3+} complex with a μ-η^1:η^1-N_2 ligand. Rhenium(III) complexes bearing PONOP, PNP^{tBu}, or $HPNP^{iPr}$ ligands have not been reported to react with N_2 until they are reduced to rhenium(II).[19-20, 32] To understand the different reactivities of **1a** and **1b** with N_2, we used density functional theory (DFT) to compare their electronic structure and their reaction with N_2. Unless otherwise stated, the reported energies were obtained at the M06/def2-TZVP level of theory in a polarizable continuum representing toluene as solvent.

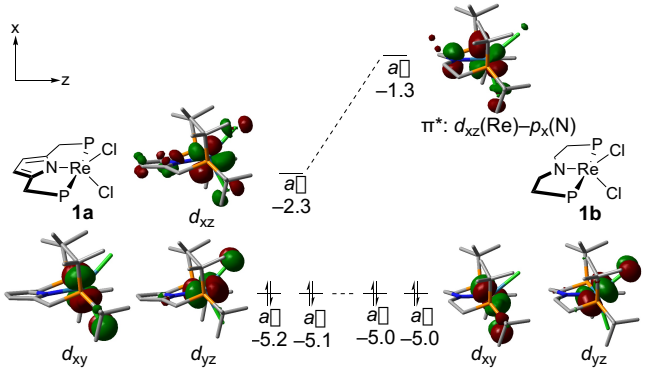

Figure 3. Frontier Kohn-Sham MOs for ^{1}**1a** and ^{1}**1b**. All energies given in eV.

Compounds **1a** and **1b** were evaluated in the lowest energy closed-shell singlet (^{1}**1a/b**) and triplet states (^{3}**1a/b**). In both complexes, the singlet state has a distorted trigonal bipyramidal geometry with the N–Re–Cl and Cl–Re–Cl angles near 140° and 110°, respectively. These angles agree with the crystallographic data available for **1b**.[18] In the given geometry, the four *d* electrons occupy a pair of nearly degenerate MOs with *a″* symmetry, which are derived from the metal d_{xy} and d_{yz} AOs with a small degree of out of phase mixing with the chloride *p* orbitals (Figure 3). The LUMO in this state has *a′* symmetry and exhibits important differences in the two complexes. The LUMO of ^{1}**1a** has d_{xz} character, along with slightly antibonding interactions with the pyrrole and

chloride ligands. In contrast, the LUMO of ^{1}**1b** is strongly π-antibonding with respect to the rhenium d_{xz} AO and the p_z orbital of the central dialkylamido nitrogen of the PNP^{tBu} ligand. This antibonding interaction is associated with the HOMO–LUMO gap of ^{1}**1b** being 1 eV larger than that of ^{1}**1a**. Consistent with the different HOMO–LUMO gaps, the triplet state from the $(a'')^2(a'')^1(a')^1$ d^4-configuration of the pyrrole complex (^{3}**1a**) is only 0.8 kcal/mol above the singlet state ^{1}**1a**, whereas ^{3}**1b** is 3.8 kcal/mol above ^{1}**1b** (Figure 4). The distorted five coordinate geometry presumably plays a role in stabilizing the closed shell state in this system.[33]

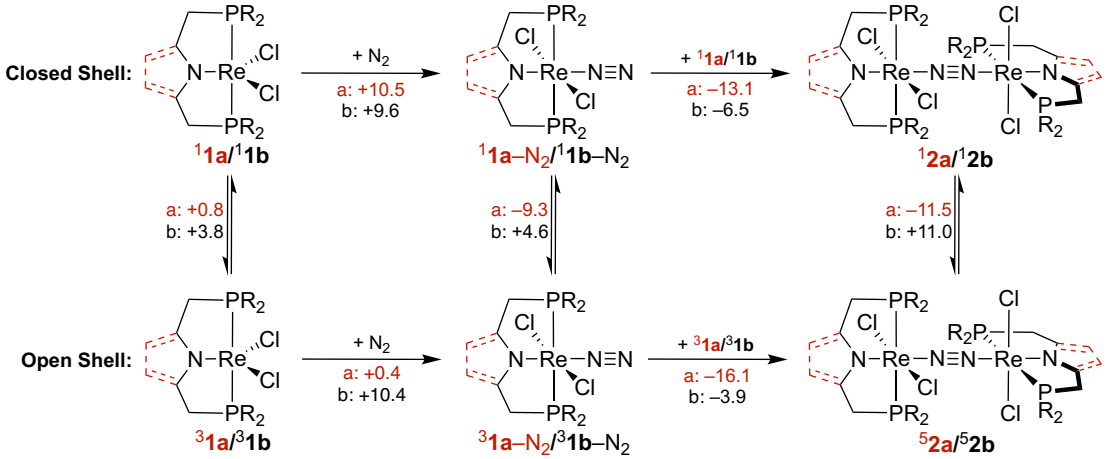

Figure 4. Computed Gibbs free energy of N_2 binding to **1a** (red) and **1b** (black) to form **2a** and **2b** in closed shell and open shell electronic configurations. Note that the experimentally observed ground state of **2a** is actually an open-shell singlet, and so the energies of the lower-right species are unlikely to be accurate. All energies given in kcal/mol.

Next, we calculated the binding of N_2 to **1a**/**b** and the formation of the terminal and bridged N_2 complexes **1a–N₂/1b–N₂** and **2a/b**, respectively (Figure 4). Although a number of electronic states are possible in the bridged N_2 complexes, we focused on the closed-shell singlet (^{1}**2**) and quintet (^{5}**2**), as well as the best match for the experimental magnetism, an open-shell singlet (^{1}**2os**) state calculated using the broken-symmetry method (Figure 5).[34]

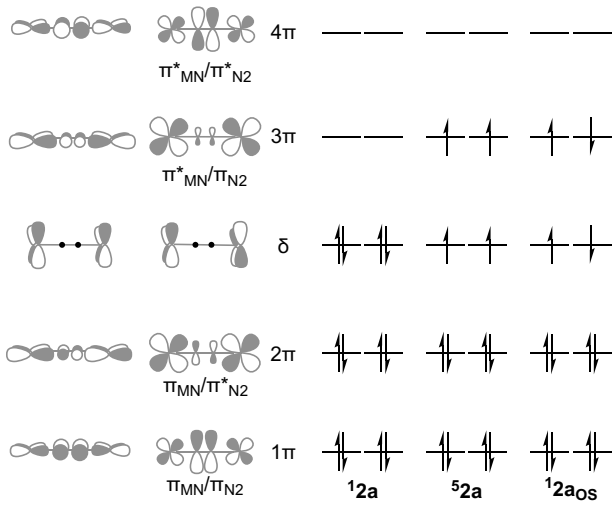

Figure 5. Qualitative MO diagram for the π/δ manifold of a bridging M–N–N–M complex in the ^{1}**2a**, ^{5}**2a**, and ^{1}**2a**$_{OS}$ states.

The octahedral complex *trans*-(P_2^{tBu}Pyrr)$ReCl_2(N_2)$ is computed to have a triplet ground state (^{3}**1a–N₂**), with nearly degenerate SOMOs (Figure S35). The singlet state (^{1}**1a–N₂**) is 9.3 kcal/mol higher in energy. The triplet configuration of ^{3}**1a–N₂** entails single occupation of an MO with Re(d_{xz})–N_2 π-bonding and N–N π-antibonding character (Figure S35, top). This MO becomes empty in ^{1}**1a–N₂**. Consistent with this model, ^{1}**1a–N₂** is computed to have a slightly shorter N–N bond length and a slightly higher N–N stretching frequency than ^{3}**1a–N₂** (Figure S35, bottom). The free energy for N_2 binding to ^{1}**1a** to give ^{3}**1a–N₂** is slightly endergonic ($\Delta G°$ = +1.2 kcal/mol; Figure 4). However, the net cooperative binding of *two* ^{1}**1a** molecules to N_2 to form ^{5}**2a** is calculated to be thermodynamically favorable ($\Delta G°$ = –14.1 kcal/mol). This result is reproduced at the M06, M06L, ωB97XD, B97-D3 and B3LYP-D3 levels. The calculated exergonic N_2 binding does not agree well with experiment, as the temperature dependent UV-Vis experiment described above implies that N_2 binding to ^{1}**1a** is reversible. In addition, the closed shell state ^{1}**2a** is computed to be 11.5 kcal/mol above the spin-aligned ^{5}**2a**, in conflict with the magnetic data. We have not

been able to determine the origin of these discrepancies, but the lack of spin-orbit coupling and configuration interaction in the DFT method may contribute.[35]

In contrast to **1a**, the product from terminal N_2 coordination to **1b**, ^{1}**1b–N$_2$** (which is experimentally unknown) is computed to have a closed shell ground state. The destabilization of the triplet state can be attributed to the strongly π-donating PNP^{tBu} ligand, which raises the energy of the d_{xz}–based SOMO. Terminal N_2 binding to ^{1}**1b** to give ^{1}**1b–N$_2$** is calculated to be endergonic by 9.6 kcal/mol. Cooperative N_2 binding to **1b** is again more favorable than terminal binding, but the computed net energy for bridging N_2 to two molecules of ^{1}**1b** remains endergonic by 3.1 kcal/mol. Thus, the greater π-donation in this complex correlates, both experimentally and computationally, with weaker N_2 binding.

N$_2$ Splitting Upon Reduction to Re^{2+}. Adding two equivalents of the reducing agent [K(18-crown-6)][$C_{10}H_8$] to **2a** at –78 °C, then warming the mixture to room temperature, yielded a dark solution containing multiple products, as determined by the ^{1}H NMR spectrum of the mixture. When the mixture was heated to 60 °C for 30 min, the color of the solution changed to orange, and ^{1}H and ^{31}P NMR spectra showed one major product in 87% spectroscopic yield (Figures S10–S11). When this reaction was performed with CoCp*$_2$ as the reducing agent instead of [K(18-crown-6)][$C_{10}H_8$], a similarly complicated reaction mixture was observed, but it converted to the same final product when heated at 70 °C for 18 h, as judged by ^{1}H and ^{31}P{^{1}H} NMR spectroscopy (Figures S12–S13). The product exhibits a single resonance in the ^{31}P {^{1}H} NMR spectrum and two sets of CH_2 and ^{t}Bu resonances in the ^{1}H NMR spectrum, indicating the loss of a mirror plane containing the phosphines when compared to **1a**. These solution phase data are consistent with a C_s-symmetric rhenium nitride product (P_2^{tBu}Pyrr)ReNCl (**3a,** Chart 1), which results from splitting the N–N bond (Scheme 3).

Scheme 3. N_2 Splitting from **2a**

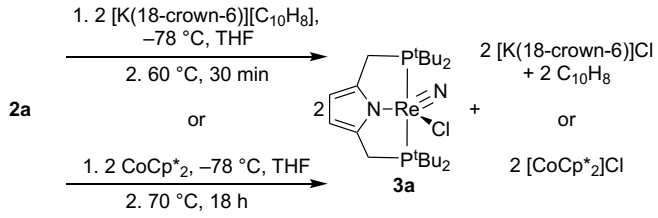

Complex **3a** was synthesized independently by treating a suspension of **2a** in THF with either tetrabutylammonium azide ($TBAN_3$) or bis(triphenylphosphine)iminium azide ([PPN][N=N=^{15}N], terminally labeled with ^{15}N), to give **3a** and **3a**$^{14/15}$**N** (50% ^{15}N enriched). The X-ray structure of **3a** has C_1 symmetry resulting from inequivalent puckering of the methylene groups. Like the solution behavior of **1a–py,** conformers of **3a** seem to interconvert on the NMR timescale. The geometry of the Re^{5+} center is nearly square pyramidal ($\tau_5 = 0.13$) and likely enforced by the strong trans influence of the Re–N triple bond (1.651(4) Å). An overlay of the infrared (IR) spectra of **3a** and **3a**$^{14/15}$**N** shows that all resonances are identical (within 2 cm^{-1}) other than the expected shift in the Re–N stretching frequency from 1070 (Re–^{14}N) to 1052 cm^{-1} (Re–^{15}N) (Figure S26). The shift is less than the calculated value from the harmonic oscillator approximation (predicted Re–^{15}N resonance 1038 cm^{-1}), suggesting that the observed band does not arise from an isolated stretching mode.

The appearance of unidentified intermediates over the course of the reaction from **2a** to **3a** has prevented detailed mechanistic investigation. Based on the hypothesis that N_2 splitting proceeds from the coordinatively unsaturated complex $[(P_2^{tBu}Pyrr)ReCl]_2(\mu\text{-}\eta^1\text{:}\eta^1\text{-}N_2)$ **(4a)** in a fashion analogous to the reaction of the isolable $[(PNP^{tBu})ReCl]_2(\mu\text{-}\eta^1\text{:}\eta^1\text{-}N_2)$ (**4b**), we explored this pathway using DFT. According to the calculations, the transformation from **2a** and two equiv of $CoCp^*_2$ into **4a** and two equiv of the ion-pair $[CoCp^*_2][Cl]$ in THF is exergonic by 12.2 kcal/mol

(Figure S36). **4a** was computed in the triplet state arising from the d^5-d^5 $(1\pi)^4(2\pi)^4(\delta)^4(3\pi)^2$ configuration of the MOs shown in Figure S38. Starting from **4a**, the activation free energy for N_2 splitting *via* the zigzag TS in the closed-shell singlet state is only 12.1 kcal/mol, and the reaction is highly exergonic (–48.8 kcal/mol) Figure S37. The corresponding activation and reaction free energies of the PNP^{tBu} complex (computed at the same level of theory as **4a**) are 25.5 and –40.8 kcal/mol, respectively, similar to the previously reported values.[18, 32] The computed barrier for the PNP^{tBu} complex is close to the experimental value of 19.8 kcal/mol determined from an Eyring plot.[32] Thus, the calculations indicate that both the kinetics and thermodynamics for N_2 splitting by **4a** to form **3a** should be even more favorable than those for **4b**. These results imply that the requirement for heating likely arises from some step other than N_2 splitting, the details of which have yet to be determined.

DISCUSSION

Typically, binding or splitting of N_2 with rhenium complexes requires reduction to the Re^{2+} oxidation state. Reduction provides a greater number of d-electrons, raises the d-orbital energies, and weakens the N–N bond through π-backbonding. The few reports of Re^{3+} complexes that can bind N_2, such as $Re(N_2)(PPh_3)(SAr)_3$ (SAr = $[SC_6H_2$-2,4,6-$^iPr_3]^-$) and $(N_3N)Re(N_2)$ (N_3N = $[(C_6F_5NCH_2CH_2)_3N]^{3-}$ or $[(C_6F_5NCH_2CH_2CH_2)_2[(C_6F_5NCH_2CH_2)N]^{3-}$), have strong π-donors as supporting ligands.[36-38] By comparison, **2a** is capable of binding N_2 in a relatively high oxidation state, and binding is *enhanced* by the weaker π-donor in $P_2^{tBu}Pyrr$ than PNP^{tBu}.

N_2 binding is tied to the spin state. The new complexes described here show that rhenium complexes of $P_2^{tBu}Pyrr$ bind N_2 at the rhenium(III) level, though the closely related complexes of PNP^{tBu} bind N_2 only at the rhenium(II) level. The $P_2^{tBu}Pyrr$ ligand is a weak π-donor that gives

ground states with open-shell configurations in the terminal and bridging Re^{3+}–N_2 complexes. In contrast, the PNP^{tBu} ligand is a stronger π-donor ligand which raises the energy of the d_{xz} AO and renders open-shell states inaccessible. The role of the spin state is illustrated in the computed results, with N_2 binding to Re^{3+} becoming more favorable in the open shell configurations of the $P_2{}^{tBu}Pyrr$ complexes. Although terminal N_2 binding to **1a** is weak, subsequent binding of a second Re^{3+} complex makes the overall binding slightly favorable.

The influence of pincer π-donation on the spin state at Re^{3+} in **1a** and **1b** is reminiscent of reported results with the isoelectronic Mo^{2+} complex, $[(PNP^{tBu})MoCl]_2(\mu\text{-}\eta^1\text{:}\eta^1\text{-}N_2)$.[15] Protonation of the pincer amides gave a doubly-protonated intermediate $[(HPNP^{tBu})MoCl]_2(N_2)^{2+}$ with an S = 2 ground state in solution. DFT studies indicated that protonation of the amides sequestered the lone pairs of the amide N atoms, and the consequent lowering in energy of the LUMO stabilizes the quintet ground state. In the rhenium system studied here, moving from PNP^{tBu} to $P_2{}^{tBu}Pyrr$ has a similar effect to protonation in the Mo system: the contribution of the *p* orbital of the central N is diminished, lowering the relative energy of the LUMO and giving rise to an open-shell configuration.

Magnetic coupling and potential coupling models. We also used temperature-dependent magnetic susceptibility studies to delve into the ground spin state and exchange coupling in **2a**. The $\chi_M T$ versus temperature plot for **2a** is near zero at low temperature, and rises with increasing temperature. Fits to the data are most consistent with a model in which two intermediate-spin (S_{Re} = 1) rhenium(III) subsites are antiferromagnetically coupled to give an open-shell singlet ground state. This is difficult to compare to the aforementioned $[(HPNP^{tBu})MoCl]_2(N_2)^{2+}$, because the former lacks structural characterization and the solution magnetic moment was measured at a single temperature.[15] Bearing these caveats in mind, the reported measurement suggests that

$[(HPNP^{tBu})MoCl]_2(N_2)^{2+}$ has an $S = 2$ ground state that differs from **2a**. Since these have the same electron configuration of $(1\pi)^4(2\pi)^4(\delta)^2(3\pi)^2$ in the π/δ manifold, it is interesting to explore why the magnetic coupling may be different. While recognizing that there are differences in the ligands, metals, and oxidation states between the Mo and Re systems, we consider two models for explaining the different magnetic coupling.

In both models, the differences in magnetic coupling are tied to the extent of charge transfer from the metal centers to N_2 (Figure 6, top). In the rhenium(III) complex **2a**, the N_2 bridge can be considered as a neutral subunit and thus the spins are localized on the rhenium centers giving rise to intermediate spin Re^{3+} ($S_{Re} = 1$) subsites. On the other hand, the formally molybdenum(II) complex $[(HPNP^{tBu})MoCl]_2(N_2)^{2+}$ has a lower formal oxidation state and a vacant coordination site trans to the bridging N_2, and is thus likely to have a more weakened N_2 bridge. Indeed, the computed geometry of $[(HPNP^{tBu})MoCl]_2(N_2)^{2+}$ in the quintet state has a lengthened N–N bond distance of 1.198 Å and NBO charge on the N_2 ligand (Table S2). Further support that $[(HPNP^{tBu})MoCl]_2(N_2)^{2+}$ has a significantly weakened N–N bond can be found in the low N–N stretching frequencies for related Mo^{n+} complexes ($n = 2$, 3, and 4).[15, 39]

In the first model (Figure 6, coupling model 1), the N_2 ligand in $[(HPNP^{tBu})MoCl]_2(N_2)^{2+}$ is treated as doubly reduced and the metals are treated as d^3 molybdenum(III) with a high-spin electronic configuration (Figure 6, top right). Note that the N_2^{2-} would be a triplet as it has two electrons in its π^* orbitals. Each of the $S_{Mo} = 3/2$ sites could be antiferromagnetically coupled to the $S = 1$ N_2^{2-}, giving alignment between the two majority Mo spins and an overall $S_{total} = 2$ ground state (Figure 6, top right), consistent with experiment. This spin alignment through mutual antiferromagnetic coupling to N_2^{2-} is like that proposed in high-spin $Fe_2(\mu\text{-}N_2)$ complexes,[40] and in the reinterpretation of the magnetic coupling in a number of other activated N_2 bridges.[31]

However, our comparative computations on ^{5}**2a** and $[(HPNP^{tBu})MoCl]_2(N_2)^{2+}$ (Table S2) show similar small amounts of β spin density on the N_2 unit, arguing against this model.

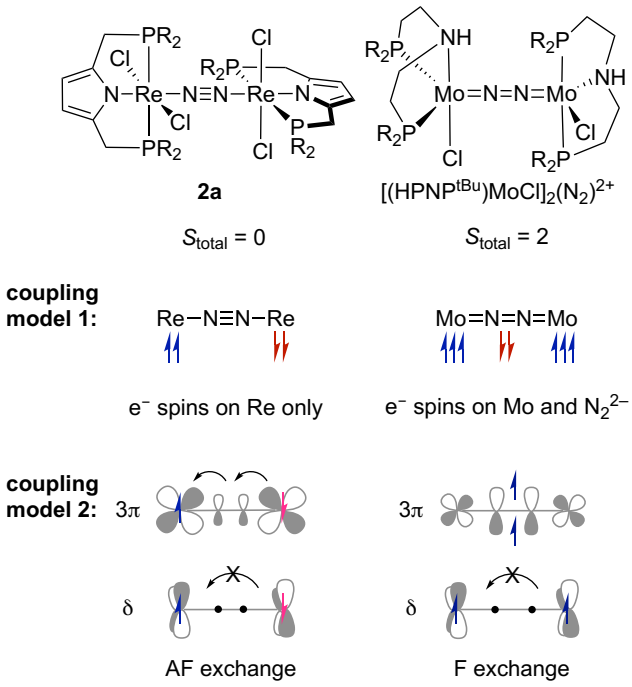

Figure 6. Two tentative models for spin interactions of **2a** and $[(HPNP^{tBu})MoCl]_2(N_2)^{2+}$. See text for explanation.

Another potential explanation is shown at the bottom of Figure 6 (coupling model 2). In **2a**, the N_2 bridge is again considered as a neutral subunit and antiferromagnetic coupling between the $S_{Re} = 1$ subsites gives the observed ground state (Figure 6, bottom left). In this model, the presence of the extra charge on N_2^{2-} in $[(HPNP^{tBu})MoCl]_2(N_2)^{2+}$ changes the nature of the 3π MO, so that it is dominated by triplet N_2^{2-} character. If the molybdenum(III) sites were low spin, all of the spin-bearing orbitals would be orthogonal to one another: the two N_2^{2-} centered spins in the 3π MO and the molybdenum centered spins in the δ MO (Figure 6, bottom right). Because none of the 3π and δ MOs have orbital overlap with one another, this would favor ferromagnetic exchange between

all four spins and could give rise to the $S = 2$ ground state. This model predicts α spin density on the N_2 unit, which also conflicts with the computations (Table S2).

Thus, our data and computations have not been able to explain the magnetic coupling. We hope that these data and models encourage future studies that explore the nature of magnetic coupling through end-on N_2 bridges.

N_2 splitting requires reduction to the rhenium(II) oxidation level. There are few published rhenium complexes capable of direct N_2 splitting, all of which require reduction to the rhenium(II) oxidation state in order to bind N_2 and acquire ten electrons in the M–N–N–M π orbital manifold.[18-20] For the systems that do not require photolysis, the reduction is also accompanied by the loss of a Cl^- ligand and the formation of complex with pseudo D_{4h} symmetry and no ligand *trans* to N_2. These bimetallic complexes are thermally unstable and proceed to the corresponding nitrido species through a zigzag transition state.[18] **2a** is an interesting case where a ten-electron configuration of the π manifold is achieved without reduction to Re^{2+}. However, N_2 splitting does not occur from **2a**, likely because the occupation of the *trans* coordination site destabilizes both the zigzag TS and the product nitride.[3] This phenomenon was previously observed in the coordinatively saturated Re^{2+} complexes bearing PONOP and $HPNP^{iPr}$ supporting ligands, as both systems require photolysis to split the N_2 ligand.[19-20] Correlation diagrams show that homolytic N_2 splitting requires two electrons from a degenerate π-MO (that is bonding with respect to the N–N bond) to pair in a σ-MO that is antibonding with respect to the N–N bond. As discussed above, the presence of a ligand trans to the bridged N_2 in **2a** raises the energy of the σ* MO (Figure S38), and the transition state for N_2 cleavage, due to the *trans* influence.[41]

CONCLUSIONS

Rhenium complexes bearing the P_2^{tBu}Pyrr pincer ligand behave differently than complexes of the related PNP^{tBu} pincers, because of the weak π-donor character of the P_2^{tBu}Pyrr ligand. This stabilizes an intermediate-spin electronic configuration, which creates more favorable Re-N_2 interactions in Re^{3+} monomers and N_2-bridged complexes. DFT computations give insight into the correlation between the ligand field strength, the electronic configuration, and the N_2 binding thermodynamics. Though these rhenium(III) N_2 complexes do not split N_2, N–N splitting to nitrides is evident upon reduction to the Re^{2+} oxidation level. This work highlights the large influence on electronic structure and N_2 reactivity of seemingly small modifications to the supporting pincer ligand.

EXPERIMENTAL SECTION

General. All manipulations were performed under an atmosphere of N_2 gas in a M. Braun glovebox or on a Schlenk line unless otherwise specified. Unless otherwise noted, all solvents were dried via passage through Q5 columns from Glass Contour Co., and stored over molecular sieves prior to use. Deuterated solvents were degassed and dried over calcium hydride before storing over molecular sieves prior to use, and THF-d_8 was dried additionally with potassium benzophenone ketyl. Pyridine (Sigma-Aldrich, 99.8%, distilled), pyrrole (Sigma-Aldrich, 98%, distilled), dimethylammonium chloride (Sigma-Aldrich, for synthesis, dissolved in chloroform and dried with molecular sieves), 1,3,5 trimethoxybenzene (Sigma-Aldrich, >99%, sublimed) and decamethylcobaltocene (Sigma-Aldrich, dissolved in pentane and filtered through Celite) were purified prior to use. $^{15}N_2$ (Cambridge Isotope Laboratories, 98+%), formaldehyde (J.T.Baker, 37% solution), sodium azide (terminal ^{15}N-labeled, Cambridge Isotope Laboratories, 98+%),

ammonium perrhenate (Sigma-Aldrich, 99+%), triphenylphosphine (Aldrich, 99%), di-tert-butylchlorophosphine (Sigma-Aldrich, 96%), and tetra-*n*-butylammonium azide (TCI Chemicals, >95%) were used without further purification. $ReCl_3(py)_2(PPh_3)$,[42] di-tert-butylphosphine,[43] 1,10-(1H-pyrrole-2,5-diyl)bis(N,N-dimethylmethanamine),[44] (Li(P^{tBu}Pyrr),[45] [PPN][N=N=^{15}N],[46] [K(18-crown-6)][$C_{10}H_8$],[47] and BPh_3[48] were synthesized from reported procedures.

Instrumentation. NMR spectra were acquired on an Agilent 400 MHz spectrometer. ^{1}H spectra were referenced to residual ^{1}H signals from the deuterated solvent with which the sample was prepared, and ^{31}P{^{1}H} NMR spectra were referenced to the corresponding ^{1}H NMR spectra using an absolute reference. Spectroscopic yields were determined using a capillary containing a solution of $SPMe_3$ or a 1,3,5-trimethoxybenzene (TMB) internal standard. UV-vis spectra were collected on a Cary 60 spectrophotometer using Schlenk-adapted quartz cuvettes with a 1 mm optical path length. Cuvettes with a 1 cm optical path length were used for variable temperature (VT) UV-Vis experiments. IR spectra were obtained using a Bruker Alpha spectrometer containing a diamond ATR unit with 2 cm^{-1} resolution. Resonance Raman (RR) spectroscopy was performed using a Horibai-Jobin Yvon HR-800 Raman Microscope equipped with a 532 nm green laser. Microcrystalline samples were irradiated open to the air or sealed in quartz capillaries; both methods resulted in identical results. Magnetic data were acquired using a Quantum Design MPMS superconducting quantum interference device. Samples were prepared by suspending microcrystalline material in Krytox® (**1a–py**) or eicosane (**2a**) inside of a polyethylene capsule. The temperature-dependent dc magnetic susceptibility was collected from 2–200 K under an applied magnetic field of 1000 Oe. Elemental analyses were obtained from the CENTC Elemental Analysis Facility at the University of Rochester. Microanalysis samples were weighed on a

PerkinElmer Model AD-6 Autobalance, analyzed on a PerkinElmer 2400 Series II Analyzer, and handled in a VAC Atmospheres argon glovebox.

***trans*-(P_2^{tBu}Pyrr)$ReCl_2$(py) (1a–py).** In a 250 mL bomb flask equipped with a magnetic stir bar Li(P_2^{tBu}Pyrr) (0.2730 g, 0.7010 mmol) and $ReCl_3(py)_2PPh_3$ (0.5024 g, 0.7046 mmol) were added using 100 mL of THF. The resulting brown mixture was sealed in the flask, removed from the glovebox, and the flask was heated at 80 °C for 4 h. During this time the mixture became homogenous and darker in color. The flask was cooled to room temperature and the volatile components of the mixture were removed using vacuum at 60 °C. In an N_2 glovebox, a minimal volume of hexane was added, and the mixture was added to a Celite cake on a fritted glass thimble. A Soxhlet extraction using 200 mL of hexanes at 100 °C for 18 hours gave a dark yellow solution, which was concentrated to dryness under vacuum to give a black residue. This residue was dissolved in toluene and layered with pentane (1:9) and stored at –40 °C. After 2 d, black needles were isolated and washed with cold pentane to give a yield of 0.3449 g (61% isolated yield over two crops). These crystals were suitable for X-ray diffraction which indicated the presence of one equiv. of toluene. **^{1}H NMR** (400 MHz, 25 °C, C_6D_6): δ 9.95 (t, 2H, *J* = 6.5 Hz, *m*-H pyridine), δ 8.88 (d, 2H, *J* = 5.5 Hz, *o*-H pyridine), δ 5.6 (br s, 36H, ^{t}Bu), δ 3.81 (t, 1H, *J* = 7.4 Hz, *p*-H pyridine), δ 2.0 (br s, 4H, CH_2), δ –13.9 (s, 2H, pyrrole) ppm. **^{31}P{^{1}H} NMR** (162 MHz, 25 °C, C_6D_6): δ –1620 ppm. **FTIR** (solid): 2966 (w), 2942 (w), 2889 (m), 2864 (m), 1476 (m), 1441 (s), 1351 (m), 1358 (s), 1215 (m), 1174 (m), 1105 (w), 1078 (m), 1019 (w), 933 (w), 829 (m), 807 (m), 760 (m), 736 (s), 670 (s), 674 (s), 572 (w), 570 (w), 487 (m), 464 (s), 452 (s) cm^{-1}. **UV-vis** (toluene, ε in $mM^{-1}cm^{-1}$): 373 (6.6), 417 (6.6), 465 (sh, 4.6) nm. **Elem. Anal.** Found(calcd) for $C_{27}H_{47}Cl_2N_2P_2Re$•0.7(C_7H_8) (%): C, 48.26(48.36); H, 6.81(6.84); N, 3.55(3.62). These values can

be attributed to the loss of some toluene when crystalline material was dried under vacuum in preparation for analysis.

[(*trans*-P_2^{tBu}Pyrr)$ReCl_2$]$_2$(μ-η^1:η^1-N_2) (2a). In an argon atmosphere, an Et_2O (6 mL) solution of **1a–py** (0.1010 g, 0.139 mmol) was added to an Et_2O (6 mL) solution of BPh_3 (0.0517 g, 0.2135 mmol) in a 50 mL bomb flask equipped with a magnetic stir bar. Over the course of 1 h the color of the solution changed from dark yellow to green, and a white precipitate formed. The solvent was removed with vacuum and the resulting green residue was dissolved in 3 mL pentane and filtered through a Celite plug. The filtrate was concentrated to 1.5 mL and the vial was transferred to an N_2 atmosphere. Toluene (1.5 mL) was added to this solution, and it was briefly sparged with N_2. This solution was stored at –40 °C overnight. Brown crystals suitable for X-ray diffraction were washed with cold pentane to give a yield of 0.0820 g (90% isolated yield). **FTIR** (solid): 3009 (w), 2997 (w), 2989 (w), 2942 (m), 2895 (m), 2864 (m), 1627 (w), 1602 (w), 1472 (s), 1455 (s), 1437 (s), 1390 (s), 1362 (s), 1311 (w), 1227 (s), 1192 (w), 1172 (s), 1109 (s), 1076 (s), 1017 (m), 997 (w), 931 (m), 833 (s), 805 (m), 762 (s), 744 (s), 727 (s), 693 (m), 660 (w), 597 (m), 572 (w), 536 (Re–^{14}N, w), 491 (m), 460 (m), 446 (s) cm^{-1}. **RR** (solid): 1862, 1819, 1719, 1234, 1067, 310, 234 cm^{-1}. **Elem. Anal.** Found(calcd) for $C_{44}H_{84}Cl_4N_4P_4Re_2$•0.26($C_7H_8$) (%): C, 42.47(41.20); H, 6.71(6.53); N, 4.02(4.22). 0.26 equiv. of toluene can be accounted for in the ^{1}H NMR spectrum of the sample sent for analysis.

[(*trans*-P_2^{tBu}Pyrr)$ReCl_2$]$_2$(μ-η^1:η^1-$^{15}N_2$) (2a–$^{15}N_2$). The same procedure for **2a** was used here except the crystallization was conducted under an atmosphere of $^{15}N_2$. **FTIR** (solid): 3007 (w), 2997 (w), 2987 (w), 2942 (m), 2895 (m), 2864 (m), 1627 (w), 1600 (w), 1472 (s), 1455 (s), 1437 (s), 1390 (s), 1362 (s), 1309 (w), 1229 (s), 1192 (w), 1172 (s), 1109 (s), 1076 (s), 1017 (m), 999 (w), 931 (m), 833 (s), 805 (m), 760 (s), 744 (s), 727 (s), 693 (m), 660 (w), 599 (m), 572 (w),

519 (Re–^{15}N, w), 491 (m), 460 (m), 446 (s) cm^{-1}. **RR** (solid): 1830, 1758, 1695, 1592, 1235, 1035, 307, 236 cm^{-1}.

(P_2^{tBu}Pyrr)$ReCl_2$ (1a). Method a: **1a–py** (0.0085 g, 0.012 mmol) and TMB were dissolved in 0.6 mL of C_6D_6, transferred to a J. Young tube charged with a glass capillary containing $SPMe_3$, and an initial ^{1}H NMR spectrum was acquired. This solution was added to a vial containing BPh_3 (0.0043 g, 0.018 mmol) and the mixture was returned to the same tube and mixed for 30 minutes. During this time the color of the solution changed from dark yellow to green which indicated the formation of **1a** (87% spectroscopic yield, ^{1}H NMR). **^{1}H NMR** (400 MHz, 25 °C, C_6D_6): δ 8.24 (d, 2H, *J* = 5.5 Hz, *o*-H pyridine, Ph_3B–py), δ 6.53 (t, 1H, *J* = 7.7 Hz, *p*-H pyridine, Ph_3B–py), δ 6.09 (t, 2H, *J* = 7.1 Hz, *m*-H pyridine, Ph_3B–py), δ 7.6 (br s, 3H, BPh_3, Ph_3B–py), δ 7.3 (br s, 9H, Ph_3B–py), δ 6.35 (s, 2H, pyrrole), δ 3.02 (vt, 4H, *J* = 3.4 Hz, CH_2), δ 1.91 (vt, 36H, *J* = 6.3 Hz, ^{t}Bu) ppm. The assignments for Ph_3B–py were based on literature reports.[49] The discrepancy between the data presented here and the literature can be attributed to an excess of BPh_3 present during the ^{1}H NMR experiment.

Method b: In a J. Young tube, C_6D_6 (1.0 mL) and a glass capillary were added to **2a** (0.0095 g, 0.0073 mmol). The tube was sonicated for 30 min and the heterogenous mixture dissolved to give a green solution. **^{1}H NMR** (400 MHz, 25 °C, C_6D_6): δ 6.35 (s, 2H, pyrrole), δ 3.02 (vt, 4H, *J* = 3.3 Hz, CH_2), δ 1.91 (vt, 36H, *J* = 6.2 Hz, ^{t}Bu) ppm. **^{31}P{^{1}H} NMR** (162 MHz, 25 °C, C_6D_6) δ –147 ppm. **UV-vis** (toluene, ε in mM^{-1}cm^{-1}): 309 (8.8), 699 (0.33), 778 (sh, 0.23) nm.

(P_2^{tBu}Pyrr)ReNCl (3a). Method a: In a 20 mL scintillation vial equipped with a magnetic stir bar**, 2a** (0.0139 g, 0.0106 mmol), $TBAN_3$ (0.0063 g, 0.022 mmol), and THF (10 mL) were stirred at 25 °C. Over the course of 2 h the slurry became orange in color and a white precipitate formed. The mixture was dried under vacuum and triturated with Et_2O (2 x 1.5 mL). The orange

product was extracted with toluene (2 x 1.5 mL). These washings were combined, filtered through Celite, and concentrated to dryness. The resulting orange powder was used without further purification and isolated in a yield (77% spectroscopic yield, ^{31}P NMR). Orange crystals suitable for X-ray diffraction were grown by layering a concentrated solution of **3a** in toluene with pentane. **^{1}H NMR** (400 MHz, 25 °C, C_6D_6): δ 6.61 (s, 2H, pyrrole), δ 2.99 (vt, 4H, J = 3.7 Hz, CH_2), δ 1.38 (vt, 18H, J = 6.8 Hz, ^{t}Bu'), δ 1.08 (vt, 18H, J = 6.8 Hz, ^{t}Bu) ppm. **^{31}P{^{1}H} NMR** (162 MHz, 25 °C, C_6D_6) δ 79 ppm. **FTIR** (solid): 2987 (w), 2944 (m), 2901 (m), 2866 (m), 1468 (m), 1392 (m), 1364 (s), 1313 (w), 1235 (m), 1180 (s), 1090 (s), 1070 (Re–^{14}N, s), 1021 (m), 935 (w), 838 (w), 821 (m), 811 (m), 752 (s), 742 (m), 668 (w), 646 (w), 613 (w), 601 (w), 583 (m), 485 (m), 462 (s), 424 (w) cm^{-1}.

Method b: In a 20 mL scintillation vial equipped with a magnetic stir bar, **2a** (0.0102 g, 0.00780 mmol) was suspended in THF (2 mL) and cooled to –78 °C. In another 20 mL scintillation vial, [K(18-crown-6)][$C_{10}H_8$] (0.0068 g, 0.016 mmol) was dissolved in THF (2 mL) and was also cooled to –78 °C. After 10 min at this temperature, the green solution of [K(18-crown-6)][$C_{10}H_8$] was added to the vial containing **2a**. This mixture was stirred at –78 °C for 10 min and then was warmed to room temperature. The solvent was removed with vacuum and the resulting black residue was dissolved in THF-d_8. This black solution was transferred to a J. Young NMR tube equipped with a capillary containing a solution of $SPMe_3$. After initial ^{31}P and ^{1}H NMR spectra were acquired, the tube was heated to 60 °C for 30 min. During this process the color of the solution changed from black to orange and final spectra were acquired (87% spectroscopic yield, ^{31}P NMR).

Method c: In a 20 mL scintillation vial equipped with a magnetic stir bar, **2a** (0.0140 g, 0.0107 mmol) was suspended in THF (2 mL) and cooled to –78 °C. In another 20 mL scintillation vial, $CoCp^*_2$ (0.0094 g, 0.029 mmol) was dissolved in THF (2 mL) and was also cooled to –78

°C. After 10 min at this temperature, the brown solution of $CoCp_2^*$ was added to the vial containing **2a**. This mixture was stirred at –78 °C for 10 min and then was warmed to room temperature. The solvent was removed with vacuum and the resulting black residue was dissolved in THF-d_8. This dark green solution was transferred to a J. Young NMR tube equipped with a capillary containing a solution of $SPMe_3$. After initial ^{31}P and ^{1}H NMR spectra were acquired, the tube was heated to 70 °C for 18 h. During this process the color of the solution changed from dark green to brown and final spectra were acquired (88% spectroscopic yield, ^{31}P NMR).

(P_2^{tBu}Pyrr)Re$^{14/15}$NCl (3a$^{14/15}$N). In a 20 mL scintillation vial, **2a** (0.0820 g, 0.0627 mmol), [PPN](N=N=^{15}N) (0.0750 g, 0.129 mmol) and THF (10 mL) were stirred at 25 °C. Over the course of 2 h the slurry became orange in color and a white precipitate formed. The mixture was dried under vacuum and triturated with Et_2O (2 x 1.5 mL). The orange product was extracted with toluene (2 x 1.5 mL). These washings were combined, filtered through Celite, and concentrated to dryness. The resulting orange powder was used without further purification and isolated in a yield of 0.0610 g (80% isolated yield). **^{1}H NMR** (400 MHz, 25 °C, C_6D_6): δ 6.62 (s, 2H, pyrrole), δ 2.98 (vt, 4H, J = 3.7 Hz, methylene H, H'), δ 1.38 (vt, 18H, J = 6.8 Hz, ^{t}Bu'), δ 1.08 (vt, 18H, J = 6.8 Hz, ^{t}Bu) ppm. **^{31}P{^{1}H} NMR** (162 MHz, 25 °C, C_6D_6) δ 79 ppm. **^{1}H NMR** (400 MHz, 25 °C, THF-d_8): δ 6.16 (s, 2H, pyrrole), δ 3.32 (m, 2H, methylene H), δ 3.22 (m, 2H, methylene H'), δ 1.55 (vt, 18H, J = 6.8 Hz, ^{t}Bu'), δ 1.22 (vt, 18H, J = 6.7 Hz, ^{t}Bu) ppm. **^{31}P{^{1}H} NMR** (162 MHz, 25 °C, THF-d_8) δ 78 ppm. **FTIR** (solid): 2989 (w), 2944 (m), 2901 (m), 2866 (m), 1466 (m), 1392 (m), 1364 (s), 1313 (w), 1235 (m), 1180 (s), 1090 (s), 1072 (Re–^{14}N, s), 1052 (Re–^{15}N, s), 1021 (m), 935 (w), 838 (w), 821 (m), 811 (m), 752 (s), 742 (m), 668 (w), 646 (w), 613 (w), 601 (w), 583 (m), 485 (m), 462 (s), 424 (w) cm^{-1}. **UV-vis** (toluene, ε in $mM^{-1}cm^{-1}$): 302 (1.5), 368 (0.49) nm. **Elem. Anal.** Found(calcd) for $C_{22}H_{42}Cl_1N_2P_2Re$ (%): C, 43.30(42.71); H,

6.88(6.84); N, 4.37(4.60). The discrepancy between the measured and calculated values is attributed to trace organic solvent.

ASSOCIATED CONTENT

Supporting Information. The following files are available free of charge.

Spectroscopy (PDF)

Calculations (MOL2)

Crystallographic information files (CIF)

AUTHOR INFORMATION

Corresponding Authors

* patrick.holland@yale.edu

Author Contributions

The manuscript was written through contributions of all authors. All authors have given approval to the final version of the manuscript.

Funding Sources

National Science Foundation (CHE-1665135 and DGE1752134)

ACKNOWLEDGMENT

The authors thank Alex Miller, Alan Goldman, James Mayer, and their research groups for valuable discussions. We thank Nicholas Bingham and Peter Schiffer for assistance with magnetometry experiments and Gannon Connor for valuable discussions. This work was funded

by the U.S. National Science Foundation (CHE-1954254). This material is based upon work supported by the National Science Foundation Graduate Research Fellowship under Grant No. DGE1752134. FH thanks URB-CNRS for support and the HPC center at AUB for computational resources.

REFERENCES

1. Foster, S. L.; Bakovic, S. I. P.; Duda, R. D.; Maheshwari, S.; Milton, R. D.; Minteer, S. D.; Janik, M. J.; Renner, J. N.; Greenlee, L. F., Catalysts for Nitrogen Reduction to Ammonia. *Nat. Catal.* **2018,** *1*, 490-500.

2. Singh, D.; Buratto, W. R.; Torres, J. F.; Murray, L. J., Activation of Dinitrogen by Polynuclear Metal Complexes. *Chem. Rev.* **2020,** *120*, 5517-5581.

3. Bruch, Q. J.; Connor, G. P.; McMillion, N.; Goldman, A. S.; Hasanayn, F.; Holland, P. L.; Miller, A. J. M., Considering Electrocatalytic Ammonia Synthesis via Bimetallic Dinitrogen Cleavage. *ACS Catal.* **2020,** *10*, 10826-10846.

4. Laplaza, C. E.; Cummins, C. C., Dinitrogen Cleavage by a Three-Coordinate Molybdenum(III) Complex. *Science* **1995,** *268*, 861-863.

5. Burgess, D. R., *NIST Chemistry WebBook*. National Institute of Standards and Technology: Gaithersburg, MD, 2017.

6. Cherry, J.-P. F.; Johnson, A. R.; Baraldo, L. M.; Tsai, Y.-C.; Cummins, C. C.; Kryatov, S. V.; Rybak-Akimova, E. V.; Capps, K. B.; Hoff, C. D.; Haar, C. M.; Nolan, S. P., On the Origin of Selective Nitrous Oxide N−N Bond Cleavage by Three-Coordinate Molybdenum(III) Complexes. *J. Am. Chem. Soc.* **2001,** *123*, 7271-7286.

7. Cui, Q.; Musaev, D. G.; Svensson, M.; Sieber, S.; Morokuma, K., N_2 Cleavage by Three-Coordinate Group 6 Complexes. W(III) Complexes Would Be Better Than Mo(III) Complexes. *J. Am. Chem. Soc.* **1995,** *117*, 12366-12367.

8. Laplaza, C. E.; Johnson, M. J. A.; Peters, J. C.; Odom, A. L.; Kim, E.; Cummins, C. C.; George, G. N.; Pickering, I. J., Dinitrogen Cleavage by Three-Coordinate Molybdenum(III) Complexes: Mechanistic and Structural Data. *J. Am. Chem. Soc.* **1996,** *118*, 8623-8638.

9. Shih, K.-Y.; Schrock, R. R.; Kempe, R., Synthesis of Molybdenum Complexes That Contain Silylated Triamidoamine Ligands. A μ-Dinitrogen Complex, Methyl and Acetylide Complexes, and Coupling of Acetylides. *J. Am. Chem. Soc.* **1994,** *116*, 8804-8805.

10. Kol, M.; Schrock, R. R.; Kempe, R.; Davis, W. M., Synthesis of Molybdenum and Tungsten Complexes That Contain Triamidoamine Ligands of the Type $(C_6F_5NCH_2CH_2)_3N$ and Activation of Dinitrogen by Molybdenum. *J. Am. Chem. Soc.* **1994,** *116*, 4382-4390.

11. Hebden, T. J.; Schrock, R. R.; Takase, M. K.; Müller, P., Cleavage of Dinitrogen to Yield a (t-BuPOCOP)Molybdenum(IV) Nitride. *Chem. Commun.* **2012,** *48*, 1851-1853.

12. Liao, Q.; Cavaillé, A.; Saffon-Merceron, N.; Mézailles, N., Direct Synthesis of Silylamine from N_2 and a Silane: Mediated by a Tridentate Phosphine Molybdenum Fragment. *Angew. Chem., Int. Ed.* **2016,** *55*, 11212-11216.

13. Arashiba, K.; Eizawa, A.; Tanaka, H.; Nakajima, K.; Yoshizawa, K.; Nishibayashi, Y., Catalytic Nitrogen Fixation via Direct Cleavage of Nitrogen–Nitrogen Triple Bond of Molecular Dinitrogen under Ambient Reaction Conditions. *Bull. Chem. Soc. Jpn.* **2017,** *90*, 1111-1118.

14. Katayama, A.; Ohta, T.; Wasada-Tsutsui, Y.; Inomata, T.; Ozawa, T.; Ogura, T.; Masuda, H., Dinitrogen-Molybdenum Complex Induces Dinitrogen Cleavage by One-Electron Oxidation. *Angew. Chem., Int. Ed.* **2019,** *58*, 11279-11284.

15. Silantyev, G. A.; Förster, M.; Schluschaß, B.; Abbenseth, J.; Würtele, C.; Volkmann, C.; Holthausen, M. C.; Schneider, S., Dinitrogen Splitting Coupled to Protonation. *Angew. Chem., Int. Ed.* **2017,** *56*, 5872-5876.

16. Solari, E.; Da Silva, C.; Iacono, B.; Hesschenbrouck, J.; Rizzoli, C.; Scopelliti, R.; Floriani, C., Photochemical Activation of the N≡N Bond in a Dimolybdenum–Dinitrogen Complex: Formation of a Molybdenum Nitride. *Angew. Chem., Int. Ed.* **2001,** *40*, 3907-3909.

17. Poveda, A.; Perilla, I. C.; Pérez, C. R., Some Considerations About Coordination Compounds With End-on Dinitrogen. *J. Coord. Chem.* **2001,** *54*, 427-440.

18. Klopsch, I.; Finger, M.; Würtele, C.; Milde, B.; Werz, D. B.; Schneider, S., Dinitrogen Splitting and Functionalization in the Coordination Sphere of Rhenium. *J. Am. Chem. Soc.* **2014,** *136*, 6881-6883.

19. Schendzielorz, F.; Finger, M.; Abbenseth, J.; Würtele, C.; Krewald, V.; Schneider, S., Metal-Ligand Cooperative Synthesis of Benzonitrile by Electrochemical Reduction and Photolytic Splitting of Dinitrogen. *Angew. Chem., Int. Ed.* **2019,** *58*, 830-834.

20. Bruch, Q. J.; Connor, G. P.; Chen, C.-H.; Holland, P. L.; Mayer, J. M.; Hasanayn, F.; Miller, A. J. M., Dinitrogen Reduction to Ammonium at Rhenium Utilizing Light and Proton-Coupled Electron Transfer. *J. Am. Chem. Soc.* **2019,** *141*, 20198-20208.

21. Venkanna, G. T.; Arman, H. D.; Tonzetich, Z. J., Catalytic C–S Cross-Coupling Reactions Employing Ni Complexes of Pyrrole-Based Pincer Ligands. *ACS Catal.* **2014,** *4*, 2941-2950.

22. Ehrlich, N.; Kreye, M.; Baabe, D.; Schweyen, P.; Freytag, M.; Jones, P. G.; Walter, M. D., Synthesis and Electronic Ground-State Properties of Pyrrolyl-Based Iron Pincer Complexes: Revisited. *Inorg. Chem.* **2017,** *56*, 8415-8422.

23. Sekiguchi, Y.; Kuriyama, S.; Eizawa, A.; Arashiba, K.; Nakajima, K.; Nishibayashi, Y., Synthesis and Reactivity of Iron–Dinitrogen Complexes Bearing Anionic Methyl- and Phenyl-substituted Pyrrole-based PNP-type Pincer Ligands Toward Catalytic Nitrogen Fixation. *Chem. Commun.* **2017,** *53*, 12040-12043.

24. Sekiguchi, Y.; Meng, F.; Tanaka, H.; Eizawa, A.; Arashiba, K.; Nakajima, K.; Yoshizawa, K.; Nishibayashi, Y., Synthesis and Reactivity of Titanium- and Zirconium-Dinitrogen Complexes Bearing Anionic Pyrrole-based PNP-Type Pincer Ligands. *Dalton Trans.* **2018,** *47*, 11322-11326.

25. Sekiguchi, Y.; Arashiba, K.; Tanaka, H.; Eizawa, A.; Nakajima, K.; Yoshizawa, K.; Nishibayashi, Y., Catalytic Reduction of Molecular Dinitrogen to Ammonia and Hydrazine Using Vanadium Complexes. *Angew. Chem., Int. Ed.* **2018,** *57*, 9064-9068.

26. Ehrlich, N.; Baabe, D.; Freytag, M.; Jones, P. G.; Walter, M. D., Pyrrolyl-Based Pincer Complexes of Iron – Synthesis and Electronic Structure. *Polyhedron* **2018,** *143*, 83-93.

27. Kawakami, R.; Kuriyama, S.; Tanaka, H.; Arashiba, K.; Konomi, A.; Nakajima, K.; Yoshizawa, K.; Nishibayashi, Y., Catalytic Reduction of Dinitrogen to Tris(trimethylsilyl)amine Using Rhodium Complexes With a Pyrrole-based PNP-type Pincer Ligand. *Chem. Commun.* **2019,** *55*, 14886-14889.

28. Tanabe, Y.; Sekiguchi, Y.; Tanaka, H.; Konomi, A.; Yoshizawa, K.; Kuriyama, S.; Nishibayashi, Y., Preparation and Reactivity of Molybdenum Complexes Bearing Pyrrole-Based PNP-Type Pincer Ligand. *Chem. Commun.* **2020,** *56*, 6933-6936.

29. Chatt, J.; Leigh, G. J.; Mingos, D. M. P., Configurations of Some Somplexes of Rhenium, Ruthenium, Osmium, rhodium, Iridium, and Platinum Halides with Mono(tertiary phosphines) and Mono(tertiary arsines). *J. Chem. Soc. (A)* **1969**, 1674-1680.

30. Pearson, C.; Beauchamp, A., ^{1}H NMR Study of Monomeric Chloro-rhenium(III) Complexes with Triarylphosphines and Nitriles. *Inorg. Chim. Acta* **1995,** *237*, 13-18.

31. Holland, P. L., Metal–Dioxygen and Metal–Dinitrogen Complexes: Where are the Electrons? *Dalton Trans.* **2010,** *39*, 5415-5425.

32. Lindley, B. M.; van Alten, R. S.; Finger, M.; Schendzielorz, F.; Würtele, C.; Miller, A. J. M.; Siewert, I.; Schneider, S., Mechanism of Chemical and Electrochemical N_2 Splitting by a Rhenium Pincer Complex. *J. Am. Chem. Soc.* **2018,** *140*, 7922-7935.

33. Rachidi, I. E.; Eisenstein, O.; Jean, Y., A theoretical study of the possible structures of d6 ML5 complexes. *New J. Chem.* **1990,** *14*, 671-677.

34. Yamanaka, S.; Kawakami, T.; Nagao, H.; Yamaguchi, K., Effective exchange integrals for open-shell species by density functional methods. *Chem. Phys. Lett.* **1994,** *231*, 25-33.

35. *Inorganic Electronic Structure and Spectroscopy*. E. I. Solomon; A. B. P. Lever, Wiley: New York, NY, 1999; Vol. 1.

36. Dilworth, J. R.; Hu, J.; Thompson, R. M.; Hughes, D. L., A d^4-Thiolato–Dinitrogen Complex. The Synthesis and Crystal Structure of $[Re(N_2)(SC_6H_2\text{-}2,4,6\text{-}Pr^i_3)_3(PPh_3)]$. *J. Chem. Soc., Chem. Commun.* **1992**, 551-553.

37. Reid, S. M.; Neuner, B.; Schrock, R. R.; Davis, W. M., Synthesis of Rhenium Complexes That Contain the $[(C_6F_5NCH_2CH_2)_3N]^{3-}$ Ligand. *Organometallics* **1998,** *17*, 4077-4089.

38. Mösch-Zanetti, N. C.; Köpke, S.; Herbst-Irmer, R.; Hewitt, M., Unsymmetrical Tren-Based Ligands: Synthesis and Reactivity of Rhenium Complexes. *Inorg. Chem.* **2002,** *41*, 3513-3520.

39. Abbenseth, J.; Oudsen, J.-P. H.; Venderbosch, B.; Demeshko, S.; Finger, M.; Herwig, C.; Würtele, C.; Holthausen, M. C.; Limberg, C.; Tromp, M.; Schneider, S., Examination of

Protonation-Induced Dinitrogen Splitting by in Situ EXAFS Spectroscopy. *Inorg. Chem.* **2020,** *59*, 14367-14375.

40. Stoian, S. A.; Vela, J.; Smith, J. M.; Sadique, A. R.; Holland, P. L.; Münck, E.; Bominaar, E. L., Mössbauer and Computational Study of an N_2-Bridged Diiron Diketiminate Complex: Parallel Alignment of the Iron Spins by Direct Antiferromagnetic Exchange with Activated Dinitrogen. *J. Am. Chem. Soc.* **2006,** *128*, 10181-10192.

41. Coe, B. J.; Glenwright, S. J., Trans-effects in octahedral transition metal complexes. *Coord. Chem. Rev.* **2000,** *203*, 5-80.

42. Rouschias, G.; Wilkinson, G., The Preparation and Reactions of Trihalogeno(alkanonitrile)bis(triphenylphosphine)rhenium(III) Complexes. *J. Chem. Soc. A* **1967**, 993-1000.

43. Yamamoto, Y.; Koizumi, T.; Katagiri, K.; Furuya, Y.; Danjo, H.; Imamoto, T.; Yamaguchi, K., Facile Synthesis of Highly Congested 1,2-Diphosphinobenzenes from Bis(phosphine)boronium Salts. *Org. Lett.* **2006,** *8*, 6103-6106.

44. Lin, K.; Chile, L.-E.; Zhen, S. C.; Boyd, P. D. W.; Ware, D. C.; Brothers, P. J., Pyrrole Pincers Containing Imidazole, Pyrazole and 1,2,4-Triazole Groups. *Inorg. Chim. Acta* **2014,** *422*, 95-101.

45. Kreye, M.; Freytag, M.; Jones, P. G.; Williard, P. G.; Bernskoetter, W. H.; Walter, M. D., Homolytic H_2 Cleavage By a Mercury-Bridged Ni(I) Pincer Complex [{(PNP)Ni}$_2${μ-Hg}]. *Chem. Commun.* **2015,** *51*, 2946-2949.

46. Connor, G. P.; Mercado, B. Q.; Lant, H. M. C.; Mayer, J. M.; Holland, P. L., Chemical Oxidation of a Coordinated PNP-Pincer Ligand Forms Unexpected Re–Nitroxide Complexes with Reversal of Nitride Reactivity. *Inorg. Chem.* **2019,** *58*, 10791-10801.

47. Castillo, M.; Metta-Magaña, A. J.; Fortier, S., Isolation of Gravimetrically Quantifiable Alkali Metal Arenides Using 18-Crown-6. *New J. Chem.* **2016,** *40*, 1923-1926.

48. Borger, J. E.; Ehlers, A. W.; Lutz, M.; Slootweg, J. C.; Lammertsma, K., Stabilization and Transfer of the Transient $[Mes^*P_4]^-$ Butterfly Anion Using BPh_3. *Angew. Chem., Int. Ed.* **2016,** *55*, 613-617.

49. Krossing, I.; Nöth, H.; Schwenk-Kircher, H., Bis(tetramethylpiperidino)aluminum Halide Adducts $tmp_2AlX \cdot Do$ and Tetrahaloaluminates of Tricoordinated Aluminum Cations $[tmp_2Al(Do)]AlX_4$. *Eur. J. Inorg. Chem.* **1998,** *1998*, 927-939.

FOR TABLE OF CONTENTS ONLY

Synopsis. The small modification of anionic N-donor on a pincer ligand causes a surprisingly large shift of N_2 reactivity in a rhenium system, leading to isolation of a dirhenium(III)-dinitrogen complex and N_2 splitting at the rhenium(II) level.

Table of Contents Graphic.